


NANO EXPRESS

Open Access



Growing gold nanostructures for shape-selective cellular uptake

Sulalit Bandyopadhyay^{1*} , Birgitte H. McDonagh¹, Gurvinder Singh², Karthik Raghunathan¹, Axel Sandvig^{3,4}, Ioanna Sandvig^{3,5}, Jens-Petter Andreassen⁶ and Wilhelm R. Glomm^{1,7}

Abstract

With development in the synthesis of shape- and size-dependent gold (Au) nanostructures (NSs) and their applications in nanomedicine, one of the biggest challenges is to understand the interaction of these shapes with cancer cells. Herein, we study the interaction of Au NSs of five different shapes with glioblastoma-astrocytoma cells. Three different shapes (nanorods, tetrahedra, and bipyramids), possessing tunable optical properties, have been synthesized by a single-step seed-mediated growth approach employing binary surfactant mixtures of CTAB and a secondary surfactant. By the use of two-step seed-mediated approach, we obtained new NSs, named *nanomakura* (*Makura* is a Japanese word used for pillow) which is reported for the first time here. Spherical Au nanoparticles were prepared by the Turkevich method. To study NS-cell interactions, we functionalized the NSs using thiolated PEG followed by 11-Mercaptoundecanoic acid. The influence of shape and concentration of NSs on the cytotoxicity were assessed with a LIVE/DEAD assay in glioblastoma-astrocytoma cells. Furthermore, the time-dependent uptake of *nanomakura* was studied with TEM. Our results indicate that unlike the other shapes studied here, the *nanomakura* were taken up both via receptor-mediated endocytosis and macropinocytosis. Thus, from our library of different NSs with similar surface functionality, the shape is found to be an important parameter for cellular uptake.

Keywords: Nanomedicine, TEM, Endocytosis, LSPR, Cytotoxicity, Drug delivery, Glioblastoma-astrocytoma

Background

Gold nanostructures (NSs) have been used in diverse biomedical applications owing to their shape- and size-dependent optical and electronic properties [1]. Au NSs display modifiable and environmentally sensitive localized surface plasmon resonance (LSPR) [2]. Au LSPR within the visible range makes them suitable candidates for biosensors and good contrast agents for computed tomography (CT) [3, 4] as well as photo-acoustic imaging [5]. NSs with even higher aspect ratios (ARs, defined as the ratio of longitudinal to the transverse dimensions) scatter light more efficiently at the longitudinal plasmon wavelength and can, therefore, perform better in optical imaging applications than spherical NPs. Smaller NSs have enhanced absorption efficiency, yielding improved efficiency in photothermal therapy [6–9]. Also, anisotropic structures have recently been used to form self-assembled structures with superior plasmonic properties

that stem from efficient quenching, extremely high molar absorptivities to development of highly localized and intense electromagnetic fields [10–13]. Being able to tune the aspect ratio and size of Au NSs, different structures can be synthesized to cater diverse applications including localized heating, sensing, encapsulating, and releasing target molecules among others [14–16].

Au NSs are typically synthesized using electrotemplating [17], photochemical reduction technique [18], or seeded growth—with or without Ag [19, 20]. In recent years, the seeded growth synthesis has become subject to further modifications, by using organic additives or binary surfactant mixtures to allow control over NS growth [21–25]. The employed synthesis conditions allow for tailoring the properties of the Au NSs by tuning their size and shape, whereby altering the scattering and absorption cross-sections of the NSs. When NSs are introduced in a biological environment, the physicochemical properties of these Au NSs (size, shape, and surface chemistry) play a vital role in cellular uptake, i.e., nanoparticle-cell interaction. Understanding of such interaction is essential to explore new biomedical applications

* Correspondence: sulalit.bandyopadhyay@ntnu.no; ratnavo@gmail.com

¹Ugelstad Laboratory, Department of Chemical Engineering, Norwegian University of Science and Technology (NTNU), N-7491 Trondheim, Norway
Full list of author information is available at the end of the article

exploiting different shaped Au NSs [26–30]. For example, Au nanorods can be employed to induce cell hyperthermia in cancer cells with the possibility to interfere with cellular functions and in some cases alter them via surface modification of the rods [30–34]. Chen et al. have reported that Au nanocages can be used for targeted photothermal destruction of breast cancer cells [35]. Also, recent reports have demonstrated that the shape of nanoparticles may be equally or more determining for cellular uptake than the size [36, 37]. This necessitates the screening of several shapes (i.e., the interaction of Au NSs of various shapes with cell) under otherwise identical conditions important to describe in vitro. To our knowledge, there exists no comprehensive study investigating the interaction of Au NSs of different shapes other than of spheres and nanorods with the cell [38, 39].

Here, we investigate the interactions of five differently shaped Au NSs with glioblastoma-astrocytoma cells and their cellular uptake. Glioblastoma multiforme (GBM) is classified as one of the most aggressive malignant human brain tumors. Patients suffering from GBM have a dismal prognosis, with a mean survival time of less than 15 months with chemotherapy and standard-of-care [40, 41]. Glioblastoma-astrocytoma is especially interesting for uptake studies not only from a medical point of view but also because of their rapid growth. Cell cultures of glioblastoma-astrocytoma have a population doubling time of 32 h and are in continuous need of extracellular nutrients. Due to this, they are highly likely to rapidly engulf foreign objects such as Au NSs, which open up, e.g., for hyperthermic tumor ablation [42], cell labeling, or drug delivery.

In the present work, five different shapes of Au NSs have been synthesized: four anisotropic NSs (nanorods—NRs, *nanomakura*—NM, tetrahedra—THH, bipyramids—BPs) by a seed-mediated growth approach using binary surfactant mixtures and spherical (SP) particles using a modified Turkevich method [43]. The shape of NSs can be tailored by varying the ratio of two different surfactants. When a two-step seed-mediated growth protocol was followed, Au *nanomakura* (*Makura* is Japanese for *pillow*) was synthesized. A two-step surface modification was performed to replace the passivating ligand with 11-mercaptoundecanoic acid (MUA) before the Au NSs were co-incubated with glioblastoma-astrocytoma cells. The effects of shape and concentration on cytotoxicity and uptake of NSs in glioblastoma-astrocytoma cells were assessed.

Experimental

Materials

Oleic acid (OA, 90%) was purchased from Alfa Aesar. Silver nitrate (AgNO_3), dodecyltrimethylammonium bromide (DDAB, 98%), chloroauric acid ($\text{HAuCl}_4 \cdot 3\text{H}_2\text{O}$, 99.999%), D-(–)-isoascorbic acid (AsA, 98%), sodium borohydride (NaBH_4 , $\geq 96\%$), 11-mercaptoundecanoic acid (MUA, 98%),

and O-[2-(3-mercaptopropionylamino) ethyl]-O-ethylpolyethylene glycol (PEG-SH) of molecular weight 5000 Da were purchased from Sigma-Aldrich. Cetyltrimethylammonium bromide (CTAB, 99%+) was purchased from Acros Organics and sodium citrate dihydrate (Na-citrate, ACS grade) from Merck. All chemicals were used as received without further purification. All solutions were prepared using distilled de-ionized water (resistivity $\sim 18.2 \mu\Omega\text{-cm}$) purified by Simplicity® Millipore water purification system.

Synthesis of anisotropic Au

Anisotropic Au NSs were synthesized using a Ag-assisted seeded growth method by employing binary surfactants (Table 1). Figure 1a shows a schematic of the synthesis method employed for the growth of NRs, THH, and BPs.

In brief, 5 mL of 0.5 mM $\text{HAuCl}_4 \cdot 3\text{H}_2\text{O}$ was first mixed with 5 mL of 0.2 M CTAB solution and allowed to stir. After that, 1.6 mL of 3.75 mM NaBH_4 was added to the mixture and allowed to react for 2 min with stirring in order to allow escape of the gas formed during the reaction. The seed solution was used for further growth, after waiting 30 min.

In a typical growth reaction, 15 mL of an aqueous mixture of CTAB and co-surfactant in various ratios was made at 80 °C as reported in Table 1. After cooling the surfactant solution to room temperature, 750 μL of 4 mM solution of AgNO_3 was added and allowed to stir for 15 min at 35 °C. This was followed by addition of 15 mL of 1 mM $\text{HAuCl}_4 \cdot 3\text{H}_2\text{O}$ solution and allowed to mix under stirring for another 15 min. After that, 135 μL of 0.063 M AsA and 96 μL of Au seeds were added, and the reaction run for 24 h at 35 °C. The products were separated using centrifugation. It is important to note that in the case of OA, the initial yellow color of the growth solution discharges within 15 min (before seed addition) indicating the reduction of Au^{3+} to Au^+ . Figure 1b shows the schematic for the synthesis of the NM, which is based on a two-seeded growth approach. The protocol followed is similar as reported above except for the addition of intermediate growth solution (300 μL) (obtained almost immediately after adding Au seeds to the first growth solution), instead of the regular seeds, to a fresh growth solution and allowing the reaction to continue for 24 h at 35 °C.

Synthesis of spherical Au NSs

Spherical Au NSs were synthesized using a modified Turkevich method [44]. In a typical synthesis, 10 mL of 10 mM sodium citrate solution was added to a 25-mL reaction flask, maintained at 70 °C. Ten milliliters of 1.5 mM chloroauric acid ($\text{HAuCl}_4 \cdot 3\text{H}_2\text{O}$) was added dropwise and allowed to react for 20 min under vigorous stirring at 70 °C. The solution turned purplish red around 8 min after the

Table 1 Moles of CTAB and co-surfactant used for the synthesis of various shapes of Au NS

Sample name	Co-surfactant	Moles of CTAB	Moles of co-surfactant
Nanorods (NRs)	OA	3.3×10^{-6}	6.3×10^{-5}
Tetrahexahedra (THH)	OA	3.3×10^{-6}	9.4×10^{-4}
Bipyramids (BPs)	DDAB	3.3×10^{-6}	4.3×10^{-4}

reaction. After that, the solution was cooled down to room temperature, and spherical Au NSs were separated from the unreacted solution, using centrifugation at 14,500 rpm for 10 min.

Surface functionalization of Au NSs

To exchange the ligands on the surface of the Au NSs, a two-step procedure adapted and modified from Thierry et al. [45] was followed. The concentrations of the as-synthesized NSs was adjusted to 1 mg mL^{-1} before the start of functionalization steps. The first step depends on the introduction of a PEG-SH layer to partially replace the bound CTAB bilayer since thiol has a greater affinity for Au surface [46]. Further, a PEG-SH layer provides steric stabilization to the NS. In the second step, the residual CTAB is replaced, and the PEG-SH layer is

further exchanged with alkanethiol, MUA. MUA allows for a complete removal of CTAB from sterically hindered PEG-SH-coated Au surface.

In a typical functionalization procedure, 1 mL of 1 mg mL^{-1} solution of the Au NS was mixed with 1 mL of 1 mg mL^{-1} solution of the PEG-SH solution. The mixed solution was kept under vigorous stirring allowing the partial replacement of CTAB with PEG-SH for 2 h. After that, PEGylated NSs were removed by centrifugation at 14,500 rpm for 20 min and redispersed in 1 mL of MQ water. To functionalize the Au NSs with carboxylic acid groups, 500 μL of the PEGylated NS solution was mixed with 250 μL of a 10 mM solution of MUA prepared in ethanol/water and allowed to react in a sonic bath maintained at 55°C for 1 h. After that, the MUA-coated Au NSs were separated from the free MUA using centrifugation at

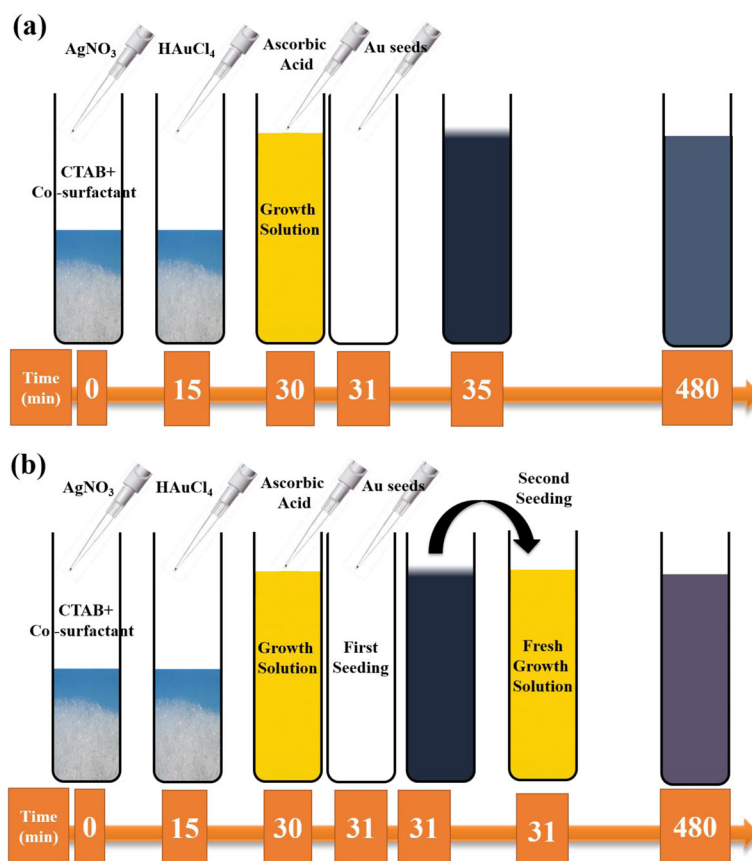


Fig. 1 Schematics of synthesis of Au NSs. **a** Schematic showing Ag-assisted seeded growth mechanism used for the synthesis of different shapes of Au NSs. **b** Schematic showing a two-seeded growth mechanism for nanomakura

14,500 rpm for 20 min. MUA-coated Au NSs were easily redispersed in MQ water.

In vitro studies

Glioblastoma-astrocytoma cell culture

Human glioblastoma-astrocytoma cells (U-87 MG, ECACC, Sigma-Aldrich, Salisbury, UK) were cultured in Eagle's Minimal Essential Medium (EMEM) with 1.25% gentamicin (Sigma) and 10% fetal bovine serum (Autogen Bioclear, Wiltshire, UK). The cultures were supplemented with 2 mM L-glutamine, 1% non-essential amino acids (NEAA, Sigma), and 1 mM sodium pyruvate (NaP, Sigma).

LIVE/DEAD® assay

A LIVE/DEAD-cell viability assay (Invitrogen, Life Technologies) evaluates the membrane integrity of cells and consists of two different dyes: calcein AM (excitation/emission 494/517 nm) and ethidium homodimer-1 (excitation/emission 517/617 nm). In live cells, intracellular esterases react with calcein AM and yield a cytoplasmic green fluorescence. Ethidium homodimer-1 (EthD-1) diffuses over damaged cell membranes of dead cells, where it binds to nucleic acids and emits red fluorescence. After labeling with NSs, LIVE/DEAD®-cell viability was performed on glioblastoma-astrocytoma cells as described by the manufacturer. Briefly, a LIVE/DEAD® solution was prepared in 4.5 mL PBS with 2.7 μL calcein (Invitrogen), and 12 μL ethidium homodimer (Invitrogen) was added at 1:1 (v/v) ratio and left to react for 30 min at 37 °C before microscopy. A nuclear stain (Hoechst 33258, excitation/emission 356/465 nm, Sigma) was added (200 $\mu\text{g mL}^{-1}$) in order to visualize the nucleus and elucidate any nuclear uptake of Au NS. Imaging was performed on an Axiovert 200 M fluorescent microscope (Zeiss, Germany), at $\times 40$ or $\times 10$ magnifications, using AxioVision Rel. 4.3 software. Images were later processed with ImageJ 1.46.

Assessing cellular toxicity based on concentration

Cells at 70% confluency were labeled with Au NS at concentrations of NS/media volume of 100 $\mu\text{g mL}^{-1}$, 200 $\mu\text{g mL}^{-1}$, 500 $\mu\text{g mL}^{-1}$, and 2 mg mL^{-1} and incubated at 37 °C for 24 h in 9-well plates (Corning®). Three parallels (wells) were prepared for each concentration. Unlabeled glioblastoma-astrocytoma cultures, at the same stage of confluence, were used as controls. The percentages of dead cells were calculated by manual counting. The highly unordered morphology of glioblastoma-astrocytoma cells makes automated counting less reliable. Three superimposed images of live and dead cells were taken in each well, and the average live and dead cells were calculated for each shape. The same was done for the blank sample, and the viability was assessed by subtracting the average dead/live of the blank.

Assessing cellular uptake as a function of time for nanomakura Au NS

Cells at 70% confluency were labeled with nanomakura Au NS at concentrations of NS/media volume of 2 mg mL^{-1} and incubated at 37 °C for 2, 6, 12, and 24 h before LIVE/DEAD® assay with nuclear stain. Unlabeled glioblastoma-astrocytoma cultures, at the same stage of confluence, were used as controls. Cell pellets were prepared for TEM via trypsination and centrifugation before primary fixation in paraformaldehyde (2% v/v) and glutaraldehyde (2.5% v/v) in PBS (0.1 M, pH = 7.4) overnight. For secondary fixation, two different fixatives were prepared for optimal staining of intracellular membranes. Both were prepared in 0.1 M cacodylate buffer, one containing 1% osmium tetroxide (v/v) and the other containing 1% osmium tetroxide (v/v) and 1.5% potassium ferrocyanide (v/v). One hour after secondary fixation at room temperature, a stepwise dehydration with alcohol was performed, before dehydration with propylene oxide, infiltration, and ultramicrotome sectioning of 70 nm slices.

Characterization techniques

Bright field (BF) STEM images were acquired using a Hitachi S-5500 electron microscope operating at 30 kV accelerating voltage. High-resolution transmission electron microscopy (HRTEM) images were acquired using JEOL 2100 operating at 200 kV. The size distributions and zeta potentials of the NSs were measured using a Malvern Zetasizer Nano-ZS instrument and the manufacturer's own software. Dynamic light scattering (DLS) measurements are based on spherical particle assumption and are not appropriate for measuring the hydrodynamic sizes of anisotropic NSs without a multi-angle setup and rigorous fitting of the resulting data. However, DLS has been used in this study as a means to qualitatively track changes in size emanating from the functionalization procedure. MQ water was used as the solvent in all cases. Ultraviolet-visible (UV-Vis) spectra were acquired with a UV-2401PC (Shimadzu) spectrophotometer. The spectra were collected over the spectral range from 200 to 800 nm. X-ray photoelectron spectroscopy (XPS) analyses were performed using a Kratos Axis Ultra DLD spectrometer (Kratos Analytical, UK), equipped with a monochromatized aluminum X-ray source (Al, $h\nu = 1486.6$ eV) operating at 10 mA and 15 kV (150 W). Survey spectra were collected over the range of 0–1100 eV binding energy with analyzer pass energy of 160 eV. A hybrid lens (electrostatic and magnetic) mode was employed along with an analysis area of approximately 300 $\mu\text{m} \times 700 \mu\text{m}$.

Results and discussion

Synthesis and characterization of anisotropic Au NSs

Anisotropic Au NSs were synthesized via a seed-mediated growth approach employing binary surfactant mixtures. When CTAB capped Au seeds (~ 5 nm) was added to the

growth solution of binary surfactant mixtures (molar ratio of OA CTAB \sim 20:1), low aspect ratio Au NRs formed (Fig. 2a, and Table 2). HRTEM image revealed the single crystalline and dog-bone morphology of NRs (inset in Fig. 2a). OA, a fatty acid that also acts as a weak reducing agent facilitates the reduction of Au^{3+} to Au^+ . The change in the color of growth solution from yellow to transparent (\sim 15 min) confirmed our observation. Further addition of ascorbic acid to the growth solution increases the reduction rate of Au^+ . As a result, Au atoms diffuse rapidly on end {111} [16] facets of the NRs because the packing of mixed micelle structures are less dense compared to the side {110} and end {100} of the NRs [25]. Therefore, the overgrowth of NRs at the end {111} facets than to side {110} and {100} facets leads to the formation of NRs of dog-bone morphology. Our results also suggest that {110} facets are unlikely to be coated with Au because of the strong interaction of these facets with surfactant molecules compared to other facets. We also confirmed the role of OA and ascorbic acid in the formation of Au NRs of dog-bone morphology.

When the concentration of OA or ascorbic acid was decreased in the growth solution, only Au NRs were obtained. These results indicate the decrease in the reduction rate and diffusion rate of gold atoms, leading to the formation of Au NRs (Additional file 1: Figure S1, ESI[†]).

When the concentration of OA relative to CTAB was increased in the growth solution (Table 1), Au NSs of elongated THH shape were obtained (Fig. 2b and Table 2). The change in the shape of Au NSs can be explained based on the modification of mixed micelle structures by OA. The rod-like mixed micelle structures are formed at a low concentration of OA. The increased amount of OA in the mixed micelle structures modifies its structure to convex and facilitate the formation of elongated THH Au NSs. Our previous study also revealed that an increase in the concentration of co-surfactant makes the mixed micelle structures more convex [25]. The shape of Au NSs can also be changed by replacing OA with DDAB. We obtained Au NSs of bipyramid (BP) shape by the use of CTAB and DDAB (Fig. 2c and Table 2) as reported in our previous work

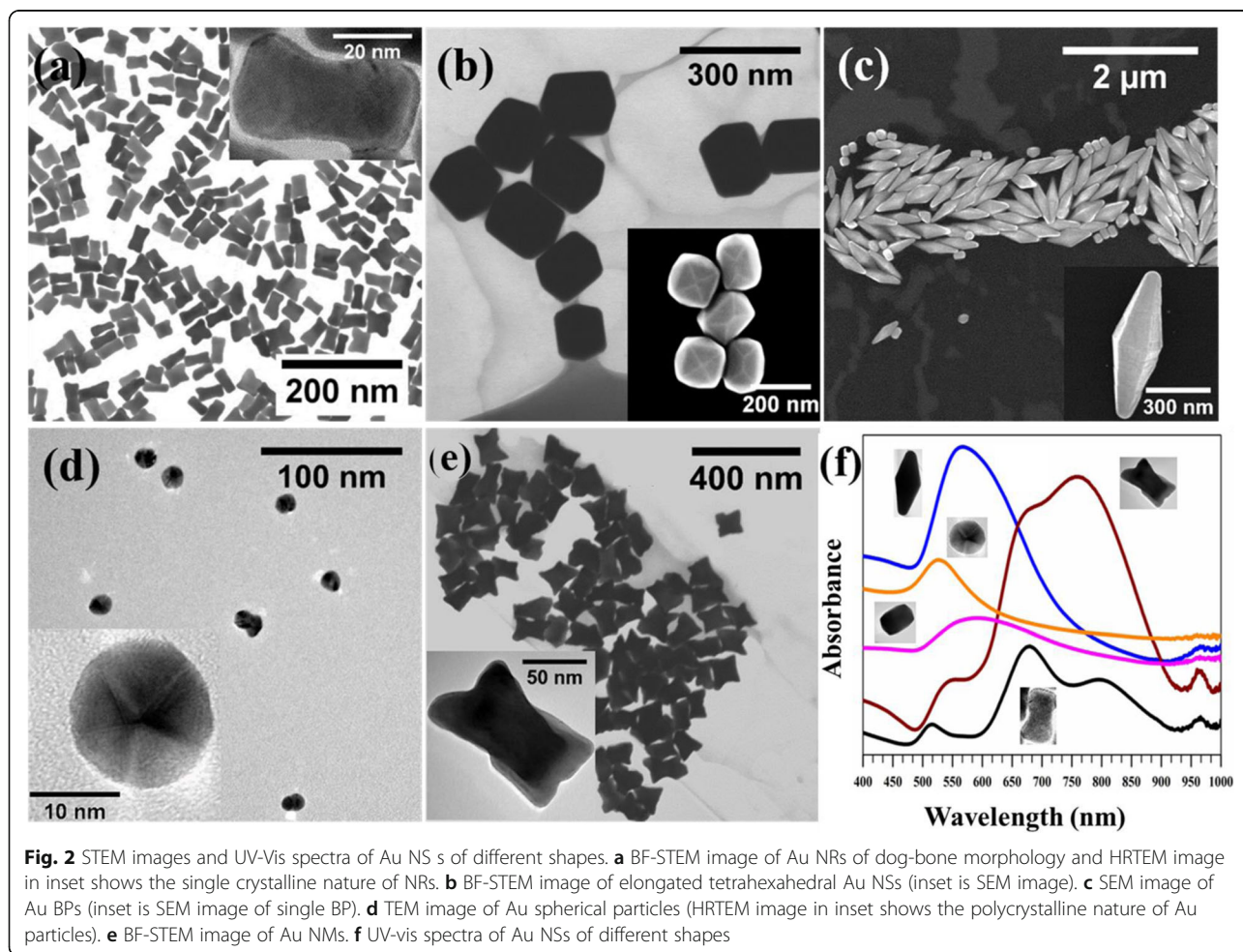


Table 2 Size distribution analysis of Au NSs of different shapes. The average size of NSs was determined from TEM images counting over 100 NSs (Additional file 1: Figure S2, ESI†). The aspect ratio (AR) is calculated as the ratio of the long axis to the short axis

Shape	Long axis (nm)	Short axis (nm)	AR
Nanorods (NRs)	45 ± 8	18 ± 6	2.8 ± 0.7
Tetrahexahedra (THH)	180 ± 25	129 ± 27	1.4 ± 0.3
Nanomakura (NM)	108 ± 15	71 ± 12	1.6 ± 0.3
Bipyramids (BPs)	644 ± 85	266 ± 19	2.4 ± 0.3
Spheres (SPs)	15 ± 4	15 ± 4	1.0 ± 0.0

[25]. Further, spherical Au particles were synthesized by a modified Turkevich method (Fig. 2d).

We also investigated the influence of seed solution on the shape of Au NSs. The seed solution was taken from the growth solution of CTAB and OA (OA:CTAB ~ 20:1) after 1 min of the reaction and added to the fresh growth solution containing OA:CTAB ~ 20:1. Au NSs of nanomakura (NM) morphology were obtained after the completion of growth reaction (Fig. 2e). The morphology of NM appears similar to dog-bone. However, since the NSs grow in all directions as shown in TEM images taken at different angles (Fig. 3a and Table 2), therefore, we call these NSs as NM. To illustrate the growth mechanism of Au NMs, a small volume was taken from the

growth solution at different time intervals and the intermediate reaction was analyzed using STEM imaging (Fig. 3b). When CTAB-coated seed particles were added to the first growth solution, the color of growth solution turned rapidly into dark violet indicating the formation of anisotropic Au NSs. A 300 μL of solution from the first growth solution was added to the second growth solution, and afterward, few drops of the solution were added to TEM grid immediately.

Representative STEM images showed relatively faster growth of Au NM in the longitudinal direction than to transverse (0 s). After 30 s, NSs resembling bow-tie configuration were seen. NM having final sizes were already observed around 3 min of the reaction. We did not see any further change in the shape and size of NSs after 30 min and 8 h. Based on our analysis, the overall growth of Au NMs can be hypothesized to be following a stochastic, “popcorn”-like autocatalytic growth mechanism, in which individual seeds lie dormant for some time before suddenly and rapidly growing into the final shapes, as has been observed for NRs by Cortie et al. [47]. The NMs have a three-dimensional structure, shown by HRTEM images of the NMs obtained at different rotation angles (Fig. 3a) unlike previously reported dog-bone-shaped NSs [48, 49].

The optical properties of the Au NSs of different shapes were measured, and the results are shown in Fig. 2f. Au NSs display tunable LSPR characteristics over the UV-Vis—visible—near-infrared (IR) range. The plasmon bands split up

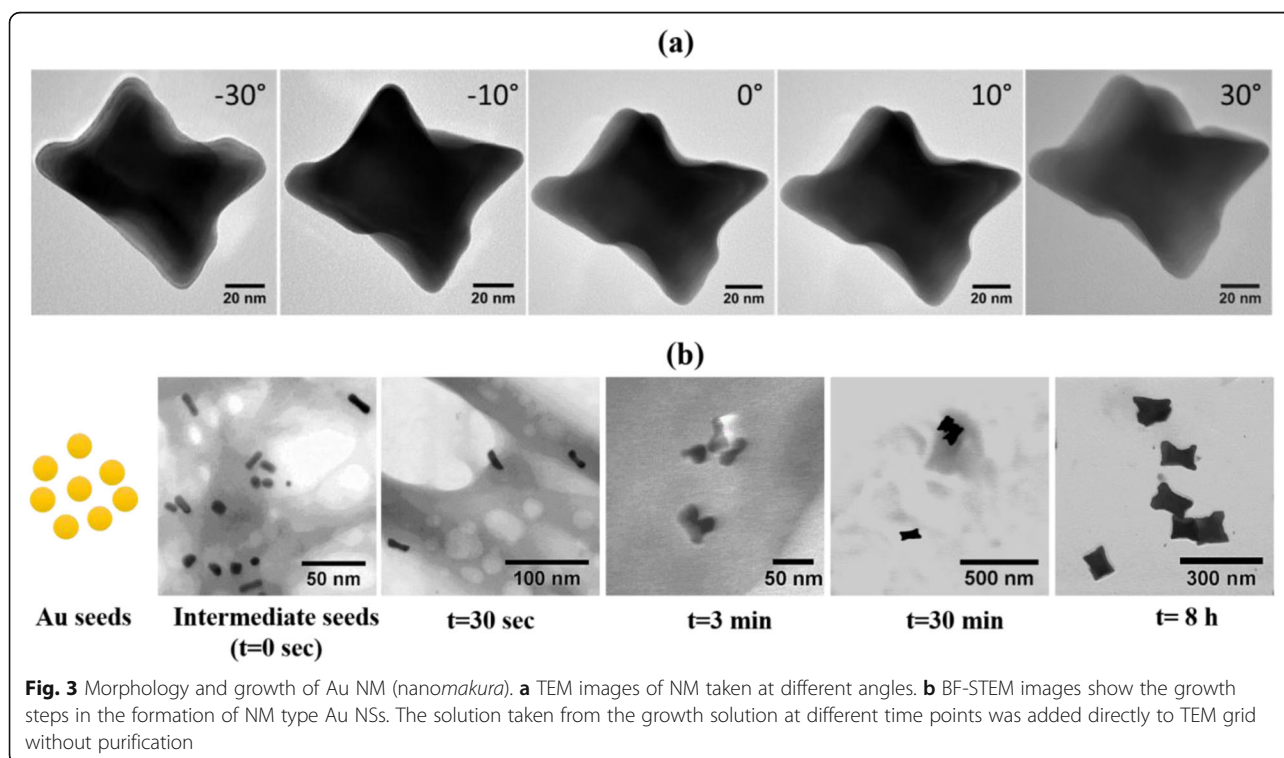


Fig. 3 Morphology and growth of Au NM (nanomakura). **a** TEM images of NM taken at different angles. **b** BF-STEM images show the growth steps in the formation of NM type Au NSs. The solution taken from the growth solution at different time points was added directly to TEM grid without purification

into multiplets for anisotropic structures—the longitudinal and transverse bands, owing to resonance oscillations along different axes. NRs show at least three distinct bands—516 nm, 679 nm, and 796 nm, the strongest being the middle one. The emergence of a third band can be associated with the polydispersity of the NRs caused due to the etching effect of oleic acid. This leads to the formation of nanorods with rough edges. Both transverse and longitudinal resonance peaks (557 and 760 nm, respectively) are observed for NM, which has a more jagged surface than the nanorods. However, for larger structures (THH and BPs), single and broad LSPR peaks are observed at 568 nm and 593 nm, respectively. While the UV-vis spectra for THH show similar resemblance to previous studies [50], the two modes for BPs seem to be fused into a broad peak unlike otherwise observed [51]. This can be attributed to a low yield of the BP shape or non-shape-selective centrifugation applied to the Au NS or an uneven coating leading to shape anisotropy in solution.

Surface functionalization of Au NSs

Au NSs of different shapes were functionalized using a two-step method—replacing the bilayer CTAB with O-[2-(3-mercaptopropionylamino) ethyl]-O-methylpolyethylene glycol (PEG-SH) and subsequently with MUA. Figure 4a shows the hydrodynamic diameters of the NSs at each stage of the functionalization. A sequential increase in the sizes is obtained when compared to CTAB-coated NSs, for each NS (except for BPs) indicating successful functionalization. As DLS measurements are based on spherical particle assumption, the size determination analysis for the anisotropic NSs must be approximated to spherical NSs having the same diffusion coefficients as that of the anisotropic NSs.

This clarifies a slight decrease in size for PEG-SH-coated BPs and also supports the UV-vis data above. As a result of the functionalization, the surface charges of the NSs decrease

massively as displayed in Fig. 4b. The cationic surfactant gets readily displaced with PEG-SH, which is further replaced by MUA owing to higher affinity towards Au surface. Owing to the small size of MUA, it has higher flexibility to displace CTAB that remains on the NSs, even after PEGylation. Final zeta potential values of MUA-coated NSs reflect negatively charged surfaces for all NSs except for NRs. This discrepancy can be linked to the uneven coating of the small NRs or their polydispersity, and the measurement principle applied. For the spherical NSs, the initial negative surface charge is due to citrate coating. However, high magnitudes of the zeta potentials for all the NSs ensure the stability of the NSs in aqueous solutions. XPS measurements carried out on the Au NSs after each stage of functionalization, i.e., with PEG-SH followed by MUA shows a very low content of bromine on the surface, confirming removal of bound CTAB in large amounts from the surfaces of the NSs. (Table 1, ESI).

Further, a coating of the NSs with PEG-SH and MUA does not change their optical characteristics dramatically. However, sequential peak broadening is obtained after functionalization for the anisotropic NSs (Additional file 1: Figure S3, ESI[†]). This can be because of different axes of rotations of the NSs due to anisotropy, non-uniform coating, size enlargement (DLS data), a polydispersity of the samples, or a combination of the above. As the optical properties of Au NSs depend on shape, surface, size, and aggregation state, so do their interactions with cells. Cell interaction studies can reveal to which extent Au NSs are taken up, their cytotoxic effects, and can point to future therapeutic and diagnostic applications.

Cellular interaction of Au NSs of different shapes

Generally, Au NSs enter the cell through endocytosis, which can be receptor-mediated or receptor-independent, through actin-dependent phagocytosis, or through other

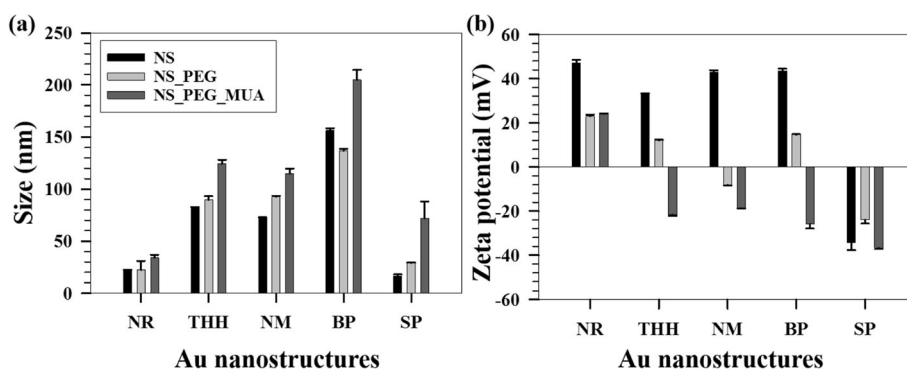


Fig. 4 Sizes and zeta potentials of Au NSs. **a** Variation of DLS sizes of the Au NSs after each stage of functionalization. **b** Variation of zeta potentials of Au NSs with each stage of functionalization. X-axis represents Au nanostructure of different shapes (NR nanorods, THH tetrahedra, NM nanomakura, BP bipyramid, SP spherical)

currently unknown endocytic routes [52]. Describing which route the NS takes is of critical importance, as it ultimately determines the NS intracellular fate [53]. Studies have shown that the mechanism of intracellular uptake depends on the physicochemical properties, AR, and the surface characteristics of the NS, as well as the cell type [54–58]. The charge of the surface stabilizing molecules will effectively be the charge of the NS [59]. Positively charged NSs have a strong protein adsorption in biological media and can severely damage the membranes of cells. Due to this, a neutral or negative charge is preferable to avoid strong adsorption on cell membranes and/or protein adsorption [26, 60]. Furthermore, the shape of NSs will determine to which extent the surface coverage of stabilizing molecules is uniform or not [61].

Here, all Au NSs, except the spherical NSs, were synthesized with the surface active agent CTAB. Au NSs were

functionalized with MUA to gain a negatively charged surface prior to the cell interaction studies. Stable MUA-coated Au NSs were subsequently co-incubated with human glioblastoma-astrocytoma cells for 24 h, and the effect of shape and concentration on cytotoxicity was assessed with a LIVE/DEAD[®] assay, supplemented with a nuclear stain to highlight intracellular Au NS.

The highest cell death was observed with the NM at high concentration (Fig. 5a), with a cell death close to 20% after blank correction. The other NSs did not show the same trend in cytotoxicity, which might indicate that NMs are taken up at a higher rate/volume than the other shapes [62]. Cell counting for these shapes showed a cytotoxicity below 5% after blank correction (for images from all shapes, see Additional file 1: Figure S4, ESI[†]).

The data presented here suggest that size plays a minor role in cytotoxicity in glioblastoma-astrocytoma cells. For

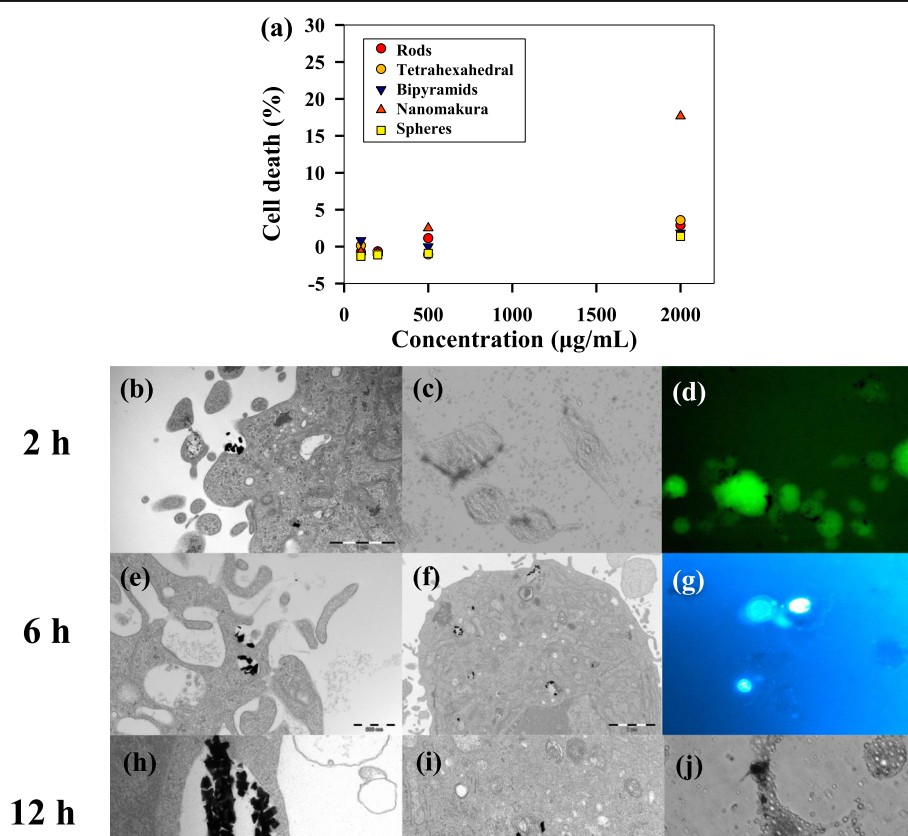


Fig. 5 Effect of Au NSs on glioblastoma-astrocytoma cells. **a** Percentage cell death of glioblastoma-astrocytoma cells as a function of concentration of AuNSs. Incubation time was 24 h. Images **b–m** are acquired after incubation of *makura*-shaped AuNSs in glioblastoma-astrocytoma cells taken at several time points up to 24 h. **b** TEM shows an invagination of the cellular membrane (m membrane, scale bar = 1 µm), and **c** halogen and **d** fluorescence images show association of makura-shaped AuNSs at the cellular membrane. **e** Uptake of makura-shaped AuNSs were observed after 6 h (scale bar = 500 nm), **f** with uptake in intracellular vesicles (v vesicle, scale bar = 2 µm). **g** Staining of the nucleus (n) suggests that makura-shaped Au NSs were excluded from the nucleus (scale bar = 500 nm), with **i** intravesicular location of makura-shaped AuNSs (vm vesicular membrane, scale bar = 500 nm). **j** Intracellular compartmentalization was also visible from the microscopy. Uptake of makura-shaped AuNSs continued at 24 h as seen in TEM images **k** (scale bar = 2 µm) and **l** (scale bar = 5 µm). **m** Detachment of glioblastoma-astrocytoma cells from the surface was observed, which most likely is an indication of cell death

instance, the small spherical NSs (15 nm) showed the same uptake/cytotoxicity as the large BPs (650/270 nm). Based on previous studies, we expected the NRs to give the highest cytotoxicity, due to their AR and surface charge. Positively charged NSs are considered to be particularly toxic as they can induce apoptosis [63] and cause the production of reactive oxygen species [64]. However, in the data presented here, the positively charged NRs did not show increased cell death compared to any other shape (Fig. 5a). This might be explained as follows: the surface charge of NS was determined with zeta potential measurements, an approach based on spherical particle assumption (Table 2). Thus, the reported charge of the NRs most likely misrepresents their actual charge. Although the AR of the rods synthesized here is large (2.8), their overall size falls in a size range that shows good uptake in cells (20–50 nm). [30, 65] A previous study has suggested that the size of NS does not only seem to govern endocytosis but also exocytosis. For instance, the removal half-life of 14 nm AuNS was much faster than removal half-life of 74 nm AuNS [26]. Here, the smaller Au rods and spheres, may, therefore, have been removed via exocytosis, which may explain their low cytotoxicity.

The main feature of the NM is not their size, but their irregular structure, and it appears from the image in Fig. 5a that shape has been the determining factor for the high uptake. However, an irregular morphology may have undermined the surface coverage of MUA and as such decreased the solution stability of the NM. Also, we cannot exclude that as two-dimensional cell studies are affected by gravity, a low stability in the cell medium increases the likelihood of sedimentation which can propel the endocytosis.

To get further insight into the uptake mechanism and interactions, we followed uptake of NM at high concentration (2 mg mL^{-1}) with light microscopy and TEM for 24 h. The images show that after 2 h of co-incubation, the NM associate with the cellular membrane (Fig. 5c, d) and are engulfed by the cells (Fig. 5b, e). The mechanism of endocytosis seems to be initially receptor-mediated (Fig. 5b) and at later stages through macropinocytosis (Fig. 5h). The latter is believed to occur when large objects enter a cell, and the aggregation of NSs may have induced macropinocytosis. This might mean that the initial solution stability of the Au NM is sufficient, but that with time they aggregate and are taken up as larger species, most likely due to protein adsorption. Uptake of any extracellular NS in an intracellular vesicle involves wrapping of the cell membrane. If many such wrapping events occur, this alters the global elasticity of the cell membrane, which in turn affects the membrane integrity. If many macropinocytosis events occur, the membrane integrity may be severely impaired. This is

believed to be one of the effects for the cytotoxicity observed for the NM.

Once inside the cell, it appears that the Au NM align at the periphery of the vesicles, adhering to the vesicular membrane (Fig. 5i). The endosome seems to be trafficked towards the nucleus (Fig. 5f, g, and l), which is consistent with previous studies that show that Au NSs taken up via receptor-mediated endocytosis may eventually end up in the Golgi apparatus [53, 66]. The uptake appears to continue upto 24 h (Fig. 5k), owing to the high concentration gradient of Au NS in the cell culture media [59].

At 24 h with co-incubation, the morphology of the cells changes (Fig. 5m), going from star-shaped to a more rounded shape with less visible filopodia [67], followed by detachment from the surface. Although this study does not go further in the molecular events following uptake of NS, a detachment of filopodia may suggest that NM can interact with the cytoskeleton and cause detachment and apoptosis.

We extended the cytotoxicity assay beyond 24 h and investigated the result of co-incubation at 48 and 72 h, the reason being that few cell studies are performed at these time points [68, 69], and the main argument being that cellular uptake reaches a plateau at 24 h [70]. Our results show (Additional file 1: Figure S5, ESI†) that beyond 24 h, the cells continued to detach from the flask surface, i.e., cell death and uptake continue beyond 24 h. As we cannot exclude that starvation of the cells would have increased the cytotoxicity and detachment, a cytotoxic response is a dynamic process likely to evolve over time differentially.

Conclusions

In summary, we have synthesized five different shapes of Au NSs using a seed-mediated growth approach (nanorods, nanomakura, tetrahedral, bipyramidal) and the Turkevich method (spherical). These NSs have different sizes: the smallest being the NRs and the largest being the BPs, ranging from 22 to 156 nm. Their optical properties measured using UV-vis spectroscopy show LSPR span from UV, visible, to near IR. High values of zeta potential render good stability in aqueous solution. With an aim to exchange the cationic surfactant on the surface, a two-step functionalization protocol was employed to replace the CTAB with PEG thiol and MUA.

After coating, the NSs showed a decrease in surface charge, coupled with an increase in size, proving successful functionalization. In vitro studies were performed for all the synthesized NSs involving co-incubation with glioblastoma-astrocytoma cells for 24 h. The greatest cytotoxic response ($\sim 20\%$) was observed with NM at high concentration, which is consistent with higher

uptake. An in--depth study with TEM revealed a time-dependent internalization in cancer cells via endocytosis and macropinocytosis. This successful internalization of the Au NM in cancer cells, coupled with their unique physicochemical properties, render them suitable for hyperthermia and drug delivery to cancer cells while being simultaneously imaged.

Additional file

Additional file 1: Figure S1. STEM image of Au NRs grown from the solution of (a) low OA concentration (i.e., OA CTAB ~ 10:1) and (b) low ascorbic acid concentration (60 μ L of 63 mM). **Figure S2.** Histograms of differently shaped AuNSs obtained from representative STEM images, showing relative population percentages of (a), (b) nanorods (NRs) (c), (d) tetrahedra (THH) (e), (f) *nanomakura* (NM) (g), (h) bipyramids (BPs), and (i) spheres (SPs). **Figure S3.** UV-Vis spectra of (a) nanorods (NRs), (b) tetrahedra (THH), (c) *nanomakura* (NM), (d) bipyramids (BPs), and (e) spheres (SPs) after each stage of functionalization. **Figure S4.** Superimposed images of differently shaped AuNSs after 24-hour co-incubation with glioblastoma-astrocytoma cells. The column to the far left show the halogen images, the middle column shows the cells stained with calcein, while the column to the far right show the superimposed images taken of the cell nuclei (white). Images (a)–(c) show glioblastoma cells incubated with nanorods (NRs), (d)–(f) spheres (SPs), (g)–(i) bipyramids (BPs), (j)–(l) tetrahedra (THH), and (m)–(o) *nanomakura* (NM). **Figure S5.** Images of *nanomakura* NSs co-incubated with glioblastoma-astrocytoma cells as a function of time. The column to the far left shows the halogen images; the middle column shows the cells stained with calcein, except image q. The column to the far right shows the superimposed images taken of the cell nuclei (white). Images (a)–(c) were taken after 2 h, (d)–(f) 6 h, (g)–(i) 12 h, (j)–(l) 24 h, (m)–(o) 48 h, and (p)–(r) 72 h of co-incubation. Images (s)–(u) show glioblastoma-astrocytoma cells not incubated with any NSs. (DOCX 2861 kb)

Abbreviations

AgNO₃: Silver nitrate; Au: Gold; BF: Bright filed; BPs: Bipyramids; CTAB: Cetyltrimethylammonium bromide; DDAB: Didecyltrimethylammonium bromide; DLS: Dynamic light scattering; EMEM: Eagle's Minimal Essential Medium; EthD-1: Ethidium homodimer-1; GBM: Glioblastoma multiforme; HAuCl₄: Chlorauric acid; HRTEM: High-resolution transmission electron microscopy; IR: Infrared; LSPR: Localized surface plasmon resonance; MUA: 11-Mercaptoundecanoic acid; Na-citrate: Sodium citrate dihydrate; NM: *Nanomakura*; NRs: Nanorods; Ns: Nanostructure; OA: Oleic acid; PEG-SH: O-[2-(3-Mercaptopropionylamino) ethyl]-O-ethylpolyethylene glycol; STEM: Scanning transmission electron microscopy; TEM: Transmission electron microscopy; THH: Tetrahedra; UV-Vis: Ultraviolet-visible; XPS: X-ray photoelectron spectroscopy

Acknowledgements

The Cellular and Molecular Imaging Core Facility (CMIC), Norwegian University of Science and Technology (NTNU) performed TEM of glioblastoma-astrocytoma cells. Authors Ioanna Sandvig and Axel Sandvig would like to acknowledge funding by the Liaison Committee between the Central Norway Regional Health Authority (RHA) and the Norwegian University of Science and Technology (NTNU) and by the EEA grant. The authors would like to thank Nan E. Torstrup Skogaker for ultramicrotome sectioning and TEM. MD David McDonagh is thanked for contributing to naming the *nanomakura*. The Research Council of Norway is acknowledged for the support to the Norwegian Micro- and Nano-Fabrication Facility, NorFab.

Authors' contributions

SB, GS, and WRG conceptualized and designed the synthesis and characterization of the NSs. JPA conceptualized and designed the mechanism investigation for the NSs. BHM, IS, and AS conceptualized and designed the cellular uptake processes. SB, GS, KR, BHM, and IS conducted the experiments. All authors contributed for analyzing and discussing the results obtained. SB, GS, BHM, WRG, and IS wrote the manuscript. All authors read and approved the final manuscript.

Competing interests

The authors declare that they have no competing interests.

Publisher's Note

Springer Nature remains neutral with regard to jurisdictional claims in published maps and institutional affiliations.

Author details

¹Ugelstad Laboratory, Department of Chemical Engineering, Norwegian University of Science and Technology (NTNU), N-7491 Trondheim, Norway. ²Department of Materials Science and Engineering, Norwegian University of Science and Technology (NTNU), N-7491 Trondheim, Norway. ³Department of Neuroscience, Norwegian University of Science and Technology (NTNU), N-7491 Trondheim, Norway. ⁴Division of Pharmacology and Clinical Neurosciences, Department of Neurosurgery, Umeå University, 901 87 Umeå, Sweden. ⁵Department of Clinical Neurosciences, University of Cambridge, England, UK. ⁶Department of Chemical Engineering, Norwegian University of Science and Technology (NTNU), N-7491 Trondheim, Norway. ⁷Polymer Particle and Surface Chemistry Research Group, SINTEF Materials and Chemistry, N-7465 Trondheim, Norway.

Received: 4 December 2017 Accepted: 8 August 2018

Published online: 28 August 2018

References

- Daniel MC, Astruc D (2004) Gold nanoparticles: assembly, supramolecular chemistry, quantum-size-related properties, and applications toward biology, catalysis, and nanotechnology. *Chem Rev* 104(1):293–346. <https://doi.org/10.1021/Cr030698>
- Murphy CJ, Thompson LB, Alkilany AM, Sisco PN, Boulos SP, Sivapalan ST, Yang JA, Chernak DJ, Huang JY (2010) The many faces of gold nanorods. *J Phys Chem Lett* 1 (19):2867–2875. <https://doi.org/10.1021/Jz100992x>
- Kim D, Park S, Lee JH, Jeong YY, Jon S (2007) Antibiofouling polymer-coated gold nanoparticles as a contrast agent for in vivo x-ray computed tomography imaging. *Nanomed Nanotechnol* 3(4):352. <https://doi.org/10.1016/j.nano.2007.10.072>
- Liu H, Xu YH, Wen SH, Chen Q, Zheng LF, Shen MW, Zhao JL, Zhang GX, Shi XY (2013) Targeted tumor computed tomography imaging using low-generation dendrimer-stabilized gold nanoparticles. *Chem-Eur J* 19 (20): 6409–6416. <https://doi.org/10.1002/chem.201204612>
- Khlebtsov N, Dykman L (2011) Biodistribution and toxicity of engineered gold nanoparticles: a review of in vitro and in vivo studies. *Chem Soc Rev* 40 (3):1647–1671. <https://doi.org/10.1039/C0cs00018c>
- Si S, Leduc C, Delville MH, Lounis B (2012) Short gold nanorod growth revisited: the critical role of the bromide counterion. *Chemphyschem* 13(1): 193–202. <https://doi.org/10.1002/cphc.201100710>
- Link S, El-Sayed MA (1999) Spectral properties and relaxation dynamics of surface plasmon electronic oscillations in gold and silver nanodots and nanorods. *J Phys Chem B* 103 (40):8410–8426. <https://doi.org/10.1021/jp9917648>
- Prescott SW, Mulvaney P (2006) Gold nanorod extinction spectra. *J Appl Phys* 99 (12):123504. <https://doi.org/10.1063/1.2203212>
- Ali MRK, Snyder B, El-Sayed MA (2012) Synthesis and optical properties of small au nanorods using a seedless growth technique. *Langmuir* 28(25): 9807–9815. <https://doi.org/10.1021/La301387p>
- Jana NR (2004) Shape effect in nanoparticle self-assembly. *Angew Chem Int Ed* 43(12):1536–1540. <https://doi.org/10.1002/anie.200352260>
- Hamon C, Novikov S, Scarabelli L, Basabe-Desmonts L, Liz-Marzán LM (2014) Hierarchical self-assembly of gold nanoparticles into patterned plasmonic nanostructures. *ACS Nano* 8(10):10694–10703. <https://doi.org/10.1021/nn504407z>
- Scarabelli L, Coronado-Puchau M, Giner-Casares JJ, Langer J, Liz-Marzán LM (2014) Monodisperse gold nanotriangles: size control, large-scale self-assembly, and performance in surface-enhanced Raman scattering. *ACS Nano* 8(6):5833–5842. <https://doi.org/10.1021/nn500727w>
- Glotzer SC, Solomon MJ (2007) Anisotropy of building blocks and their assembly into complex structures. *Nat Mater* 6(7):557–562
- Chen WQ, Weng SN, Zhang F, Allen S, Li X, Bao LW, Lam RHW, Macoska JA, Merajver SD, Fu JP (2013) Nanoroughened surfaces for efficient capture of circulating tumor cells without using capture antibodies. *ACS Nano* 7(1): 566–575. <https://doi.org/10.1021/nn304719q>

15. Alam R, Lightcap IV, Karwacki CJ, Kamat PV (2014) Sense and shoot: simultaneous detection and degradation of low-level contaminants using graphene-based smart material assembly. *ACS Nano* 8(7):7272–7278. <https://doi.org/10.1021/nn502336x>
16. Moyano DF, Rotello VM (2011) Nano meets biology: structure and function at the nanoparticle interface. *Langmuir* 27(17):10376–10385. <https://doi.org/10.1021/la2004535>
17. Hulteen JC, Martin CR (1997) A general template-based method for the preparation of nanomaterials. *J Mater Chem* 7(7):1075–1087. <https://doi.org/10.1039/A700027h>
18. Kim F, Song JH, Yang PD (2002) Photochemical synthesis of gold nanorods. *J Am Chem Soc* 124 (48):14316–14317. <https://doi.org/10.1021/Ja028110o>
19. Gole A, Murphy CJ (2004) Seed-mediated synthesis of gold nanorods: role of the size and nature of the seed. *Chem Mater* 16 (19):3633–3640. <https://doi.org/10.1021/Cm0492336>
20. Sau TK, Murphy CJ (2004) Room temperature, high-yield synthesis of multiple shapes of gold nanoparticles in aqueous solution. *J Am Chem Soc* 126 (28):8648–8649. <https://doi.org/10.1021/Ja047846d>
21. Ye XC, Zheng C, Chen J, Gao YZ, Murray CB (2013) Using binary surfactant mixtures to simultaneously improve the dimensional tunability and monodispersity in the seeded growth of gold nanorods. *Nano Lett* 13(2):765–771. <https://doi.org/10.1021/Nl304478h>
22. Lai JP, Zhang L, Niu WX, Qi WJ, Zhao JM, Liu ZY, Zhang W, Xu GB (2014) One-pot synthesis of gold nanorods using binary surfactant systems with improved monodispersity, dimensional tunability and plasmon resonance scattering properties. *Nanotechnology* 25 (12):125601. <https://doi.org/10.1088/0957-4484/25/12/125601>
23. Ye XC, Gao YZ, Chen J, Reifsnnyder DC, Zheng C, Murray CB (2013) Seeded growth of monodisperse gold nanorods using bromide-free surfactant mixtures. *Nano Lett* 13 (5):2163–2171. <https://doi.org/10.1021/Nl400653s>
24. Singh G, van Helvoort ATJ, Bandyopadhyay S, Volden S, Andreassen JP, Glomm WR (2014) Synthesis of Au nanowires with controlled morphological and structural characteristics. *Appl Surf Sci* 311:780–788. <https://doi.org/10.1016/j.apsusc.2014.05.162>
25. Bandyopadhyay S, Singh G, Glomm WR (2017) Shape tunable synthesis of anisotropic gold nanostructures through binary surfactant mixtures. *Mater Today Chem* 3 :1–9. <https://doi.org/10.1016/j.mtchem.2016.11.005>
26. Chithrani BD, Chan WCW (2007) Elucidating the mechanism of cellular uptake and removal of protein-coated gold nanoparticles of different sizes and shapes. *Nano Lett* 7(6):1542–1550. <https://doi.org/10.1021/nl070363y>
27. Cho EC, Xie JW, Wurm PA, Xia YN (2009) Understanding the role of surface charges in cellular adsorption versus internalization by selectively removing gold nanoparticles on the cell surface with a $i-2/ki$ etchant. *Nano Lett* 9(3):1080–1084. <https://doi.org/10.1021/Nl803487r>
28. Sonavane G, Tomoda K, Makino K (2008) Biodistribution of colloidal gold nanoparticles after intravenous administration: effect of particle size. *Colloid Surface B* 66 (2):274–280. <https://doi.org/10.1016/j.colsurfb.2008.07.004>
29. Cho EC, Au L, Zhang Q, Xia YN (2010) The effects of size, shape, and surface functional group of gold nanostructures on their adsorption and internalization by cells. *Small* 6 (4):517–522. <https://doi.org/10.1002/sml.200901622>
30. Chithrani BD, Ghazani AA, Chan WC (2006) Determining the size and shape dependence of gold nanoparticle uptake into mammalian cells. *Nano Lett* 6(4):662–668
31. Kang B, Mackey MA, El-Sayed MA (2010) Nuclear targeting of gold nanoparticles in cancer cells induces DNA damage, causing cytokinesis arrest and apoptosis. *J Am Chem Soc* 132(5):1517–1519. <https://doi.org/10.1021/ja9102698>
32. Dickerson EB, Dreaden EC, Huang X, El-Sayed IH, Chu H, Pushpanketh S, McDonald JF, El-Sayed MA (2008) Gold nanorod assisted near-infrared plasmonic photothermal therapy (pPPT) of squamous cell carcinoma in mice. *Cancer Lett* 269(1):57–66
33. Wang L, Liu Y, Li W, Jiang X, Ji Y, Wu X, Xu L, Qiu Y, Zhao K, Wei T, Li Y, Zhao Y, Chen C (2011) Selective targeting of gold nanorods at the mitochondria of cancer cells: implications for cancer therapy. *Nano Lett* 11(2):772–780. <https://doi.org/10.1021/nl103992v>
34. Eghtedari M, Liopo AV, Copland JA, Oraevsky AA, Motamedi M (2009) Engineering of hetero-functional gold nanorods for the in vivo molecular targeting of breast cancer cells. *Nano Lett* 9(1):287–291. <https://doi.org/10.1021/nl802915q>
35. Chen J, Wang D, Xi J, Au L, Siekkinen A, Warsen A, Li Z-Y, Zhang H, Xia Y, Li X (2007) Immuno gold nanocages with tailored optical properties for targeted photothermal destruction of cancer cells. *Nano Lett* 7(5):1318–1322
36. Barua S, Yoo J-W, Kolhar P, Wakankar A, Gokarn YR, Mitragotri S (2013) Particle shape enhances specificity of antibody-displaying nanoparticles. *Proc Natl Acad Sci* 110(9):3270–3275. <https://doi.org/10.1073/pnas.1216893110>
37. Liu Y, Tan J, Thomas A, Ou-Yang D, Muzykantov VR (2012) The shape of things to come: importance of design in nanotechnology for drug delivery. *Ther Deliv* 3(2):181–194
38. Malugin A, Ghandehari H (2010) Cellular uptake and toxicity of gold nanoparticles in prostate cancer cells: a comparative study of rods and spheres. *J Appl Toxicol* 30(3):212–217. <https://doi.org/10.1002/jat.1486>
39. Alkilany AM, Murphy CJ (2010) Toxicity and cellular uptake of gold nanoparticles: what we have learned so far? *J Nanopart Res* 12(7):2313–2333. <https://doi.org/10.1007/s11051-010-9911-8>
40. Clark MJ, Homer N, O'Connor BD, Chen Z, Eskin A, Lee H, Merriman B, Nelson SF (2010) U87mg decoded: the genomic sequence of a cytogenetically aberrant human cancer cell line. *PLoS Genet* 6(1):e1000832. <https://doi.org/10.1371/journal.pgen.1000832>
41. Johnson DR, O'Neill BP (2012) Glioblastoma survival in the United States before and during the temozolomide era. *J Neuro-Oncol* 107(2):359–364. <https://doi.org/10.1007/s11060-011-0749-4>
42. Verma J, Lal S, Van Noorden CJF (2014) Nanoparticles for hyperthermic therapy: synthesis strategies and applications in glioblastoma. *Int J Nanomedicine* 9(1):2863–2877. <https://doi.org/10.2147/IJN.S57501>
43. Turkevich J, Stevenson PC, Hillier J (1951) A study of the nucleation and growth processes in the synthesis of colloidal gold. *Discuss Faraday Soc* 11:55
44. Bandyopadhyay S, Singh G, Sandvig I, Sandvig A, Mathieu R, Kumar PA, Glomm WR (2014) Synthesis and in vitro cellular interactions of superparamagnetic iron nanoparticles with a crystalline gold shell. *Appl Surf Sci* 316:171–178. <https://doi.org/10.1016/j.apsusc.2014.07.081>
45. Thierry B, Ng J, Krieg T, Griesser HJ (2009) A robust procedure for the functionalization of gold nanorods and noble metal nanoparticles. *Chem Commun* 13:1724–1726
46. Shaw CF (1999) Gold-based therapeutic agents. *Chem Rev* 99 (9):2589–2600. <https://doi.org/10.1021/Cr980431o>
47. Edgar JA, McDonagh AM, Cortie MB (2012) Formation of gold nanorods by a stochastic “popcorn” mechanism. *ACS Nano* 6(2):1116–1125. <https://doi.org/10.1021/nn203586j>
48. Gou L, Murphy CJ (2005) Fine-tuning the shape of gold nanorods. *Chem Mater* 17(14):3668–3672. <https://doi.org/10.1021/cm050525w>
49. Chen HJ, Shao L, Li Q, Wang JF (2013) Gold nanorods and their plasmonic properties. *Chem Soc Rev* 42(7):2679–2724. <https://doi.org/10.1039/c2cs35367a>
50. Yin PG, You TT, Tan EZ, Li J, Lang XF, Jiang L, Guo L (2011) Characterization of tetrahedral gold nanocrystals: a combined study by surface-enhanced raman spectroscopy and computational simulations. *J Phys Chem C* 115(37):18061–18069. <https://doi.org/10.1021/Jp2041586>
51. Qi HB, Bi N, Chen YH, Zheng X, Zhang HQ, Wang X, Chen Y, Tian Y (2011) Determination of DNA based on localized surface plasmon resonance light scattering using unmodified gold bipyramids. *Spectrochim Acta A* 81 (1):769–773. <https://doi.org/10.1016/j.saa.2011.07.023>
52. Kunzmann A, Andersson B, Thurnherr T, Krug H, Scheynius A, Fadeel B (2011) Toxicology of engineered nanomaterials: focus on biocompatibility, biodistribution and biodegradation. *Biochim Biophys Acta Gen Subj* 1810 (3):361–373. <https://doi.org/10.1016/j.bbagen.2010.04.007>
53. Canton I, Battaglia G (2012) Endocytosis at the nanoscale. *Chem Soc Rev* 41(7):2718–2739. <https://doi.org/10.1039/c2cs15309b>
54. Dykman LA, Khlebtsov NG (2014) Uptake of engineered gold nanoparticles into mammalian cells. *Chem Rev* 114(2):1258–1288. <https://doi.org/10.1021/cr300441a>
55. Chu Z, Zhang S, Zhang B, Zhang C, Fang CY, Rehori I, Cigler P, Chang HC, Lin G, Liu R, Li Q (2014) Unambiguous observation of shape effects on cellular fate of nanoparticles. *Scientific Reports* 4 :4495. <https://doi.org/10.1038/srep04495>
56. Cartiera MS, Johnson KM, Rajendran V, Caplan MJ, Saltzman WM (2009) The uptake and intracellular fate of PLGA nanoparticles in epithelial cells. *Biomaterials* 30(14):2790–2798. <https://doi.org/10.1016/j.biomaterials.2009.01.057>
57. Gratton SEA, Ropp PA, Pohlhaus PD, Luft JC, Madden VJ, Napier ME, DeSimone JM (2008) The effect of particle design on cellular internalization pathways. *Proc Natl Acad Sci* 105(33):11613–11618. <https://doi.org/10.1073/pnas.0801763105>

58. Huff TB, Hansen MN, Zhao Y, Cheng JX, Wei A (2007) Controlling the cellular uptake of gold nanorods. *Langmuir* 23(4):1596–1599. <https://doi.org/10.1021/la062642r>
59. Chithrani DB (2010) Intracellular uptake, transport, and processing of gold nanostructures. *Mol Membr Biol* 27(7):299–311. <https://doi.org/10.3109/09687688.2010.507787>
60. McDonagh BH, Volden S, Lystvet SM, Singh G, Ese M-H, Ryan JA, Lindgren M, Sandvig A, Sandvig I, Glomm WR (2015) Self-assembly and characterization of transferrin-gold nanoconstructs and their interaction with bio-interfaces. *Nanoscale* 7(17):8062–8070. <https://doi.org/10.1039/C5NR01284H>
61. Bartczak D, Muskens OL, Nitti S, Sanchez-Elsner T, Millar TM, Kanaras AG (2012) Interactions of human endothelial cells with gold nanoparticles of different morphologies. *Small* 8(1):122–130. <https://doi.org/10.1002/sml.201101422>
62. Yen H-J, Hsu S-H, Tsai C-L (2009) Cytotoxicity and immunological response of gold and silver nanoparticles of different sizes. *Small* 5(13):1553–1561. <https://doi.org/10.1002/sml.200900126>
63. Arvizo RR, Miranda OR, Thompson MA, Pabelick CM, Bhattacharya R, Robertson JD, Rotello VM, Prakash YS, Mukherjee P (2010) Effect of nanoparticle surface charge at the plasma membrane and beyond. *Nano Lett* 10(7):2543–2548. <https://doi.org/10.1021/nl101140t>
64. Wang F, Bexiga MG, Anguissola S, Boya P, Simpson JC, Salvati A, Dawson KA (2013) Time resolved study of cell death mechanisms induced by amine-modified polystyrene nanoparticles. *Nanoscale* 5(22):10868–10876. <https://doi.org/10.1039/C3NR03249C>
65. Jiang W, KimBetty YS, Rutka JT, ChanWarren CW (2008) Nanoparticle-mediated cellular response is size-dependent. *Nat Nano* 3(3):145–150. http://www.nature.com/nano/journal/v3/n3/supinfo/nano.2008.30_S1.html
66. Mosesson Y, Mills GB, Yarden Y (2008) Derailed endocytosis: an emerging feature of cancer. *Nat Rev Cancer* 8(11):835–850. <https://doi.org/10.1038/nrc2521>
67. Hoa NT, Ge L, Erickson KL, Kruse CA, Cornforth AN, Kuznetsov Y, McPherson A, Martini F, Jadus MR (2015) Fascin-1 knock-down of human glioma cells reduces their microvilli/filopodia while improving their susceptibility to lymphocyte-mediated cytotoxicity. *Am J Transl Res* 7(2):271–284
68. Coradeghini R, Gioria S, García CP, Nativo P, Franchini F, Gilliland D, Ponti J, Rossi F (2013) Size-dependent toxicity and cell interaction mechanisms of gold nanoparticles on mouse fibroblasts. *Toxicol Lett* 217(3):205–216
69. Sandvig I, Hoang L, Sardella TCP, Barnett SC, Brekken C, Tvedt K, Berry M, Haraldseth O, Sandvig A, Thuen M (2012) Labelling of olfactory ensheathing cells with micron-sized particles of iron oxide and detection by MRI. *Contrast Media Mol Imaging* 7(4):403–410. <https://doi.org/10.1002/cmmi.1465>
70. Soenen SJ, Manshian B, Montenegro JM, Amin F, Meermann B, Thiron T, Cornelissen M, Vanhaecke F, Doak S, Parak WJ, De Smedt S, Braeckmans K (2012) Cytotoxic effects of gold nanoparticles: a multiparametric study. *ACS Nano* 6(7):5767–5783. <https://doi.org/10.1021/nn301714n>

Submit your manuscript to a SpringerOpen[®] journal and benefit from:

- Convenient online submission
- Rigorous peer review
- Open access: articles freely available online
- High visibility within the field
- Retaining the copyright to your article

Submit your next manuscript at ► springeropen.com
